Extreme Mechanics Letters 30 (2019) 100504

Contents lists available at ScienceDirect

Extreme Mechanics Letters

journal homepage: www.elsevier.com/locate/eml

Voltage-controlled morphing of dielectric elastomer circular sheets into conical surfaces

Ehsan Hajiesmaili [*,1], Eesha Khare [1], Alex Chortos [1], Jennifer Lewis, David R. Clarke

School of Engineering and Applied Sciences, Harvard University, Cambridge, MA 02138, United States

ARTICLE INFO

Article history:
Received 9 April 2019
Received in revised form 17 June 2019
Accepted 18 June 2019
Available online 26 June 2019

ABSTRACT

Dielectric elastomers provide large, fast, and reversible deformations which can be harnessed to provide predefined sophisticated actuation deformations. This paper describes a method, fabrication technique and analysis tools for morphing flat sheets of dielectric elastomers into conical shapes upon applying a voltage, using a set of concentric, stiff rings that are 3D-printed onto a multilayer elastomer sheet. A finite elements user-subroutine and a simple analytical model are developed to predict the actuation profile, both showing excellent agreement with the experimental measurements. The actuation force of the dielectric elastomer actuator is measured as a function of the applied voltage and displacement and estimated using the analytical and numerical models. Finally, a few examples of dielectric elastomers with other designs of the 3D-printed stiffening elements and their actuation shapes are demonstrated.

1. Introduction

Large elastic deformations can be produced in soft elastomeric materials by the application of an electric field through their thickness which, in turn, causes lateral expansion of the elastomer sheet due to the incompressibility of the elastomer [1]. This simple biaxial expansion provides the basis for many existing actuators that utilize linear expansion–contraction or bending to be used for devices such as artificial muscles [2], airships [3], and fish-like robots [4]. However, the same underlying mechanism provides new opportunities for the design and fabrication of novel devices that can generate more complex actuation deformations and morph their shape — a feature that the traditional actuators such as electrical motors cannot provide easily. Tunable lenses [5], haptic devices [6], peristaltic pumps [7], and soft grippers [8] are examples of devices that use dielectric elastomers to generate nontrivial actuation deformations and provide new functionalities. Further advancements of the actuation mechanisms of dielectric elastomer actuators can result in shape-morphing actuators for novel applications ranging from shape-changing airfoils that morph their surface to alter the fluid flows, to shape-changing mannequins that can change their shape to show how a piece of clothing would look on different body types. Such nontrivial actuation deformations and shape-morphing of dielectric elastomers can be accomplished through two mechanisms. The first is to incorporate inhomogeneous or anisotropic mechanical stiffness, through methods such as including stiff fibers into the elastomer sheet [8], halftone lithography [9], or writing localized direction of molecular order in liquid crystal elastomers [10,11]. The second mechanism is to create inhomogeneous electric field inside the elastomer which causes inhomogeneous actuation and reconfigurable shape-morphing [12].

In this work, we demonstrate that a disk of a dielectric elastomer with a set of concentric stiff rings on its surface can morph from a flat surface into a three-dimensional conical surface upon applying a voltage. This is in marked contrast to the actuation without the rings, where the dielectric elastomer simply expands radially without moving out-of-plane. Although many geometric arrangements of stiffening elements can be devised, the selection of concentric stiff rings in this work is based on a simple concept, namely that a set of concentric rings constrains the electric field induced elastomer deformation to be radial. To accommodate the radial expansion of the elastomer, it must deflect out of plane producing a cone shape. A flat sheet of elastomer that morphs from a flat sheet into a cone, upon applying a voltage, could be used for applications such as a tactile display or a tunable airfoil surface that modifies the air flow and drag forces across it.

To demonstrate the shape morphing concept and to show that it is consistent with expectation we present both experimental validation and finite element predictions of the actuation shapes as a function of the applied voltage for actuators with different spacings of the rings. First, the materials and fabrication of a multilayer dielectric elastomer with 3D-printed concentric rings

* Corresponding author.
E-mail address: hajiesmaili@seas.harvard.edu (E. Hajiesmaili).

[1] Theses authors contributed equally to this work and should be considered co-first authors.

https://doi.org/10.1016/j.eml.2019.100504
2352-4316/

is presented in the following section. A multilayer dielectric elastomer is employed to decrease the actuation voltages that must be applied, and the concentric rings are 3D-printed to ensure concentricity. After describing the materials and methods, a finite elements user-subroutine is developed to predict the actuation profile as a function of the applied voltage and geometrical and material properties. These are compared with experimental measurements in the following section. The blocking force of the actuator is measured as a function of the displacement and the applied voltage. After presenting the results, the effect of the material and geometrical parameters on the actuation displacements and forces are discussed. In addition, based on the experimental findings and the numerical results, it is shown that a simple analytical model can also be used to predict both the detailed actuation shape and the deformations as a function of voltage. Finally, a few examples of the shape morphing of dielectric elastomers with other designs of the 3D-printed stiffening elements are demonstrated.

2. Materials and methods

2.1. Materials and fabrication

A multilayer dielectric elastomer actuator, consisting of several elastomer layers separated by inter-digited compliant electrodes, shows in-plane lateral expansion when a voltage is applied to its two sets of electrodes. To morph into a cone shape, the actuator consists of a multilayer circular disk of elastomer with internal inter-digited compliant electrodes and an external set of stiff concentric rings 3D-printed onto its surface, shown schematically in Fig. 1a. Fig. 1b shows an optical image of such dielectric elastomer actuator with ten 3D-printed concentric rings.

The fabrication process consists of creating a multilayer dielectric elastomer sheet [13] by repetition of spin-coating and UV-curing of a precursor, masking and stamping of a CNT-based compliant electrode, and 3D-printing of a set of stiff rings onto the surface of the multilayer elastomer sheet, as explained in further details in the following.

First, an elastomer layer was made by spin-coating of an acrylic precursor at 2000 rpm for 1 min and UV curing for 180 s under an array of 6 Hitachi F8T5-BL UV lamps with peak intensity at 366 nm wavelength. The precursor consisted of 99% CN9028 (Sartomer Arkema Group), an aliphatic urethane acrylate oligomer, and 1% benzophenone as photoinitator. The thickness of each elastomer layer was 61 ± 2 μm, measured over 12 samples, when the precursor was at 21 °C.

Then, a compliant electrode was created onto the elastomer sheet by placing a mask onto the elastomer, stamping a mat of carbon nanotubes onto the mask, and removing the mask. The mask, defining the geometry of the electrode, had a circular shape with diameter of 30 mm. To create the mat of carbon nanotubes [14], 600 μl of dispersion of functionalized single-walled carbon nanotubes (P3-SWNT, Carbon Solutions, Inc.) in deionized water with resistivity of 18 MΩ.cm was vacuum-filtered onto a porous PTFE filter membrane (T020A090C, Advantec MFS, Inc.) through a filtration area of 38.5 cm^2. Typical mass concentration of the carbon nanotubes in deionized water is 20 to 25 mg/l [15], characterized by the transmittance of the dispersion: 17% transmittance at 550 nm wavelength with reference to the deionized water. The mat of carbon nanotubes was then heat treated for 2 h at 110 °C under 150 Torr vacuum, in order to increase the robustness and electrical breakdown strength of the actuator [2].

The fabrication process was continued by repeating the spin-coating, UV-curing, masking, and stamping steps for the required number of elastomer layers and electrodes. The actuators studied in this paper consisted of 12 elastomer layers, separated by 11 compliant electrodes. This results in ten active layers and a top and bottom elastomer layer for protection. The outer edge of the actuator was then cut from the multilayer elastomer sheet using a CO2 laser cutter. The diameter of the elastomer disk was 31 mm and the electrodes had a diameter of 30 mm so as to form a passive (unelectroded) rim of 0.5 mm width at the edge.

The rings were written on the top elastomer sheet by a 3D printing technique. The ink was prepared by combining 45.4 wt% Ebecryl 8413, 45.4 wt% pentaerythritol tetraacrylate, 7.3 wt% silica (EH-5 from Cabot Corporation), and 1.9 wt% 2,2-Dimethoxy-1,2-diphenylethan-1-one. The mixture was speed-mixed for 40 min to create a homogeneous ink, loaded into 3 cc syringe barrels, and centrifuged for 20 min to remove air bubbles. The stiff features were printed using 100 μm nozzles (Nordson EFD) at a print speed of 1.2 mm/s and a pressure of 427 PSI. The stiff features were cured under nitrogen for 60 s using an Omnicure S2000 at 20% power. Confocal imaging of the 3D-printed rings shows that the cross-section of the rings is a circular segment with width of 200 μm and height of 50 μm, supplementary figure S1d.

Electrical connection to the electrodes was made by first cutting the electrode connection parts with a razor blade and then brushing a conductive carbon paste (Carbon Conductive Adhesive 502, Electron Microscopy Sciences) onto the cut to make direct contact with the electrodes.

2.2. Characterization

The mechanical properties of the elastomer were characterized using uniaxial stretch tests on dogbone samples. The dogbone samples were fabricated by repeating the spin-coating and UV-curing steps 10 times, followed by CO2 laser cutting of a dogbone shape (ASTM D412-16, die C scaled by half) out of the elastomer sheet. For the uniaxial stretch test, the dogbone samples were clamped to two linear stages (GHC SLP35, GMC Hillstone Co. and MicroFlex e100 servo drive) and stretched at a constant rate of 0.1 mm/s. To measure the stretch, two lines were drawn onto the narrow part of the dogbone sample, 15 mm apart, and their distance was measured optically using a camera placed 20 cm away from the sample. As the sample was stretched, the tensile force was measured using a loadcell (FUTEK LSB200, 2 lb, JR S-Beam loadcell) mounted onto one of the clamps. The stress–stretch curve of the elastomer is shown in supplementary figure S1a, as well as the Gent model fitted to the data. Fitting the Gent model to the measured stress–stretch curve yields a shear modulus of 327 ± 5 kPa, averaged over 6 samples, and strain hardening parameter of $J_{\text{lim}} = 5.7 \pm 0.5$. Having J_{lim} smaller than 7 leads to a monotonic voltage–strain curve for the actuator and helps to prevent electromechanical instability [16].

The mechanical properties of the stiff acrylic, used for 3D-printing of the rings, were also characterized using uniaxial stretch tests. Slabs of stiff acrylic, 0.6 mm in thickness and 5.5 mm in width, were 3D-printed and UV-cured for 60 s. The slab was clamped onto two linear stages (GHC SLP35, GMC Hillstone Co. and MicroFlex e100 servo drive), stretched at a constant rate of 0.1 mm/s, while the force was measured using a loadcell (FUTEK LSB200, 50 lb, JR S-Beam loadcell). The shear modulus was extracted from the stress–stretch curve, shown in the supplementary figure S1c, by fitting the neo-Hookean model to the initial linear part of the curve at strain smaller than 1%. The measured shear modulus is 136 ± 6 MPa, averaged over 5 samples.

Electrical properties of the system were characterized by measuring the permittivity spectrum of thin sheets of elastomer through the airgap method using a Keysight E4980A LCR meter and a Keysight 16451B Dielectric Test Fixture. The relative permittivity of the elastomer, averaged over 5 samples, ranges

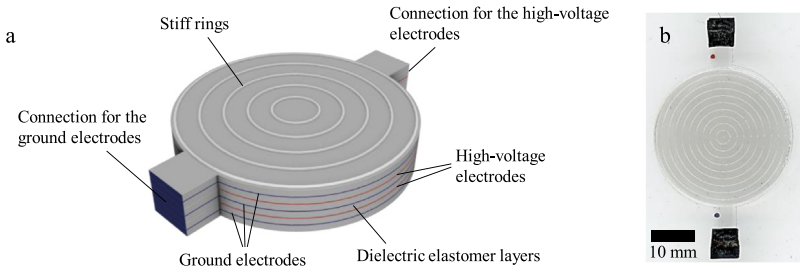

Fig. 1. Schematic of the design of dielectric elastomer actuators with 3D-printed concentric stiff rings. (a) A multilayer dielectric elastomer actuator with concentric stiff rings consisting of six elastomer layers separated by three low-voltage electrodes and two high-voltage electrodes, shown in blue and red, respectively, and five concentric stiff rings that are 3D-printed onto the top layer. The schematic representation is not up to scale; typically, the thickness of each elastomer layer is in the order of tens of micrometers and the lateral dimensions are in the orders of centimeters. (b) an optical image of the fabricated dielectric elastomer actuator with ten concentric rings.

from 6.2 at 20 Hz to 4.9 at 2 MHz, as shown in the supplementary figure S1b. For the smaller frequencies, where the profile measurements are performed, the effect of the interfacial polarizations could lead to a larger relative permittivity [17]. Therefore, for the numerical and analytical models, the relative permittivity is considered as a fitting parameter and a value of 8 is used.

The three-dimensional actuation profiles were measured optically using a laser line scanner (MTI ProTrak PT-G 60-40-58) that measures height, z, as a function of x position, and a linear stage (GHC SLP35, GMC Hillstone Co. and MicroFlex e100 servo drive) that moves the sample in y direction. To aid in the profile measurements, the dielectric elastomer sheets were coated with an anti-glare powder (3D anti-glare scan spray, Helling GmbH). The profile measurements were performed while the electrodes of the actuators are connected to a high-voltage power supply (Trek 610E, Trek Inc.), and the voltage was ramped up stepwise with steps of 50 volts.

To measure the actuation forces, the voltage was ramped up from 0 to 2.5 kV in steps of 50 volts, in each step a stiff plate was pressed onto the actuator, and the reaction force was measured using a loadcell (FUTEK LSB200, 2 lb, JR S-Beam loadcell), as shown in the Supplementary video 2. This results in a two-dimensional map of actuation force versus the applied voltage and the displacement.

3. Numerical model

To complement the experimental studies, fully-coupled finite elements analyses were performed. These were used to visualize stress and strain profiles, to study how the ring stiffness and spacing affects the actuation deformation, and to predict the actuation shape for DEAs with different configurations of the stiffening elements. Following the standard finite element formulation procedure [18], the governing partial differential equations are converted into a system of nonlinear algebraic equations. This system of nonlinear equations was solved in Abaqus using Newton–Raphson's iterative method with an Abaqus user element (UEL) developed to incorporate the coupling terms into the residual vector and stiffness matrix.

Actuation of dielectric elastomers is mathematically described by the balance of momentum and the Gauss's flux theorem, together with material constitutive models and a proper set of boundary conditions. For quasi-static actuation, the indexical form (summed on the repeating index) of the equation of balance of momentum in the current configuration is given by $\partial\sigma_{ij}/\partial x_i + b_j = 0$, where σ_{ij} is the Cauchy stress tensor and b_j is the vector of electrostatic body force per volume. The body forces could also be expressed in terms of the Maxwell stress tensor, ${\sigma_{ij}}^{\text{Max}}$, and the balance of momentum in terms of the Maxwell stress tensor becomes $\frac{\partial}{\partial x_i}.\left(\sigma_{ij} + {\sigma_{ij}}^{\text{Max}}\right) = 0$ with $j = 1, 2, 3$.

For the mechanical constitutive equation of the elastomer and the stiff fibers, a nearly incompressible neo-Hookean model is adopted, which expresses the material's Helmholtz-free energy, ψ, as a function of the first and the third invariants of the Cauchy–Green deformation tensors, I_1 and I_3: $\psi = \frac{\mu}{2}\left(\bar{I}_1 - 3\right) + \kappa\,(J-1)^2$ where $\bar{I}_1 = I_1/I_3^{1/3}$ and $J = \sqrt{I_3}$. The shear modulus, μ, of the elastomer and fibers were assigned to be 327 kPa, and 136 MPa respectively, based on our measurements. Their bulk modulus, κ, was assumed to be two orders of magnitude larger than their shear modulus in order to represent nearly incompressible materials. This corresponds to a Poisson's ratio of 0.495. The Cauchy stress tensor σ_{ij} and the left Cauchy–Green deformation tensor $B_{ij} = F_{ik}F_{jk}$ ($F_{ij} = \frac{\partial x_i}{\partial X_j}$ being the deformation gradient tensor) are related through the Helmholtz free energy: $\sigma_{ij} = \frac{2}{J}\frac{\partial\psi}{\partial I_1}B_{ij} + \frac{2}{J}\frac{\partial\psi}{\partial I_3}I_3\delta_{ij}$ with $i, j = 1, 2, 3$. where δ_{ij} is the Kronecker delta. The mechanical deformation is coupled to the electric field through the Maxwell stress tensor. For an incompressible material with linear polarization, the Maxwell stress tensor is determined by the electric field E_i, and the relative permittivity of the elastomer ϵ_r, as ${\sigma_{ij}}^{\text{Max}} = \epsilon_0\epsilon_r\left(E_iE_j - \frac{1}{2}E_kE_k\delta_{ij}\right)$.

Distribution of electric displacement vector D_i is described by the Gauss's flux theorem, $\partial D_i/\partial x_i = q$, where q is the density of free charges. For the dielectric material model, we use a linear polarization constitutive equation, leading to the electric displacement D_i being a linear function of the electric field: $D_i = \epsilon_0\epsilon_r E_i$ for $j = 1, 2, 3$.

The two governing partial differential equations, the constitutive models, and the appropriate boundary condition equations fully describe the actuation of dielectric elastomers. Following the standard finite elements formulation procedure, this system of partial differential equations is written in integral form and a shape function N^A is considered for the weights w and the solution variables — displacement u_i and electric potential ϕ. The integration was performed using Gaussian quadrature. This procedure converts the set of partial differential equations into the following $4N$ system of nonlinear algebraic equations (N being the total number of the nodes):

$$\begin{Bmatrix} R^A_{u_j} \\ R^A_{\phi} \end{Bmatrix} = \begin{Bmatrix} -\sum_{n_G}\left(\sigma_{ij} + {\sigma_{ij}}^{\text{Max}}\right)\frac{\partial N^A}{\partial x_i}w_{n_G}\det\frac{\partial x_p}{\partial\xi_q} \\ \quad + \sum_{n_G}\left(t_jN^A\right)w_{n_G}\det\frac{\partial x_p}{\partial\xi_q} \\ -\sum_{n_G}\left(D_i\frac{\partial N^A}{\partial x_i} + qN^A\right)w_{n_G}\det\frac{\partial x_p}{\partial\xi_q} \\ \quad + \sum_{n_G}\left(q_sN^A\right)w_{n_G}\det\frac{\partial x_p}{\partial\xi_q} \end{Bmatrix} = \begin{Bmatrix} 0 \\ 0 \end{Bmatrix}$$

For $j = 1, 2, 3$ and $A = 1, \ldots, N$. This set of nonlinear algebraic equations was solved iteratively using Newton–Raphson's method:

$$\begin{Bmatrix} R^A_{u_j} \\ R^A_{\phi} \end{Bmatrix}^{i+1} = \begin{Bmatrix} R^A_{u_j} \\ R^A_{\phi} \end{Bmatrix}^{i} + \frac{\partial}{\partial u^B_k} \begin{Bmatrix} R^A_{u_j} \\ R^A_{\phi} \end{Bmatrix}^{i} \delta u^B_k + \frac{\partial}{\partial \phi^B} \begin{Bmatrix} R^A_{u_j} \\ R^A_{\phi} \end{Bmatrix}^{i} \delta \phi^B = \begin{Bmatrix} 0 \\ 0 \end{Bmatrix},$$
$$j = 1, 2, 3, \quad A = 1, \ldots, N$$

where the superscripts $i + 1$ and i are the iteration number. This can be rewritten in the familiar finite elements form involving stiffness matrix and residual vector:

$$\begin{bmatrix} K_{u^A_j u^B_k} & K_{u^A_j \phi^B} \\ K_{\phi^A u^B_k} & K_{\phi^A \phi^B} \end{bmatrix} \begin{Bmatrix} \delta u^B_k \\ \delta \phi^B \end{Bmatrix} = \begin{Bmatrix} R^A_{u_j} \\ R^A_{\phi} \end{Bmatrix}, \quad j = 1, 2, 3, \quad A = 1, \ldots, N$$

An Abaqus user element (UEL) was developed to incorporate the coupling terms $K_{u^A_j \phi^B}$ and $K_{\phi^A u^B_k}$ into the element stiffness matrix, and the Maxwell stress term into the element residual vector. The solution variables u^B_k and ϕ^B are obtained by solving this system of linear algebraic equations iteratively until the residual vector and change of the solution variables are within a convergence criterion.

4. Results and discussion

Initially flat, multilayer elastomer sheets with concentric stiff rings morph out of plane to produce an axi-symmetric shape when a voltage is applied to their inter-digitated electrodes. An example is shown in Fig. 2 and supplementary video 1, for a 31 mm diameter and 0.73 mm thick sheet, consisting of 12 elastomer layers with equally spaced concentric rings that are 1 mm apart, before and after applying 3 kV to its inter-digited electrodes. The shape changes are reversible, as shown in the supplementary video 1; when the voltage is reduced to zero, the elastomer sheet returns to being flat. The actuation height profile and the Gaussian curvature profile of the actuator at 3 kV is shown in Fig. 2c and d, respectively, showing characteristics of a cone surface: the contour lines of the height profile are equally-spaced concentric circles, and the Gaussian curvature profile has a large positive value at the center and is negligible elsewhere.

To study how the spacing between the concentric rings affects the actuation shape and displacement, dielectric elastomers with 3, 5, 10, and 15 equally-spaced concentric rings were fabricated, resulting in ring-spacings of 5.0, 3.0, 1.5, and 1.0 mm, respectively. Fig. 3a shows photographs of the actuation of dielectric elastomers with 5.0 mm and 1.5 mm ring-spacings at 0 to 3 kV applied voltages. As the voltage is increased, all actuators morph into a cone shape whose height increases with the applied voltage, with no significant differences in their shape and displacement. Fig. 3b shows the cross-section profiles, defined as the intersection of the actuation profile and a vertical plane passing through the axis of the cone, for the actuators with the four different ring-spacings of 1.0, 1.5, 3.0, and 5.0 mm. One of the major results of these studies is that the actuation profiles, at the same applied voltage, falls on one curve for each of the actuators despite the different ring-spacings. This intriguing result is attributed to two effects. First, as the stiffness of the rings is nearly three orders of magnitude larger than that of the elastomer, only a few rings, with large spacing between them, are needed to constrain the azimuthal deformation. Secondly, since the width of the rings is much smaller than the spacing between them, the radial deformation is not affected by the number of the rings. Therefore, regardless of their spacing, the rings introduce anisotropy but not inhomogeneity, provided that the stiffness of the rings is much larger than the elastomer and the width of the rings is much smaller than their spacing. This is consistent with the findings of the finite element simulations. Furthermore, Fig. 3c shows that the displacement of the tip of the cone is also the same for all the actuators with different ring-spacings. It is also notable that the vertical displacements can be large, appreciable fractions of the sheet diameter. For instance, the vertical displacement of a 31 mm diameter, 0.73 mm thick elastomer sheet with 15 equally-spaced concentric rings can be as high as 8 mm, under an applied voltage of 3 kV.

Using the finite element user-subroutine, described in Numerical Analysis, the actuation profile of a dielectric elastomer with 1 mm ring-spacing is analyzed and compared to the experimental measurements of the profile. The finite element model uses the experimentally measured shear modulus and layer thickness of 327 kPa and 61 μm, respectively. For the relative permittivity a value of 8 is used, as a fitting parameter. The cross-section of the rings is modeled as a segment of a circle with width of 200 μm and height of 50 μm, using the confocal image of a 3D-printed ring shown in the supplementary figure S1. Fig. 4a shows finite elements analysis of the actuation profile of dielectric elastomer sheets with ring-spacings of 1 to 5 mm, under an applied voltage of 3 kV. The finite elements analysis of the actuation profiles at different voltages are compared to the experimental measurements of the actuation profiles in Fig. 4b, showing an excellent agreement between the two. Fig. 4c shows the finite elements results for the displacement of the center of the actuator disk as a function of the applied voltage, compared to that of the experimental measurements.

The finite elements modeling is also employed to analyze the state of the strain of the actuators. Fig. 4d shows the first, second, and third principal strains on the cross-section of a dielectric elastomer with 1 mm ring-spacing actuated at 3 kV. The first principal strain is in radial direction and has an order of magnitude of 15% for the most part of the actuator. The third principal strain is in the thickness direction and compressive due to coulombic attraction of the opposite charges on the inter-digited electrodes and has an order of magnitude of −15%. The second principal strain, however, is negligible compared to the lateral and through-thickness strains, over most part of the actuator. This confirms that the actuation is uniaxial. Also, the strains do not change significantly along the disk of elastomer, except near the center of the disk, which confirms that the actuation is homogeneous. The observation that the strains through the thickness are almost constant also suggests that the bending effects could be neglected. This deformation state and the resulting shape changes agree with the predictions of the nonlinear elasticity of incompatible surface growth [19]: a flat surface morphs into a cone when the azimuthal stretch is constrained, the radial strain is positive, and the bending terms are negligible.

Based on the observations that the actuated shape is a conical surface as well as the findings of the finite element computations, it was found that a simplified analytical model could be used to estimate the actuation displacements and forces. Four assumptions are made: (a) the actuation shape is a cone, (b) the deformation is uniaxial, (c) the bending terms are negligible, and (d) the radial displacement is completely confined because of the high stiffness of the rings. The two assumptions regarding the uniaxial actuation strains and negligible bending terms are confirmed by the numerical analysis.

The uniaxial lateral stretch, λ, of a dielectric elastomer sheet could be derived by the minimization of the total potential energy, W, which is the sum of the strain energy of the deformed elastomer sheet, electrostatic energy of the charged dielectric elastomer actuator, and the work potential of the charging unit:

$$W = \pi R^2 m t_0 \left(\frac{\mu}{2} (I_1 - 3) \right) + \pi R^2 n t_0 \left(\frac{1}{2} \epsilon E^2 \right) - q\phi$$

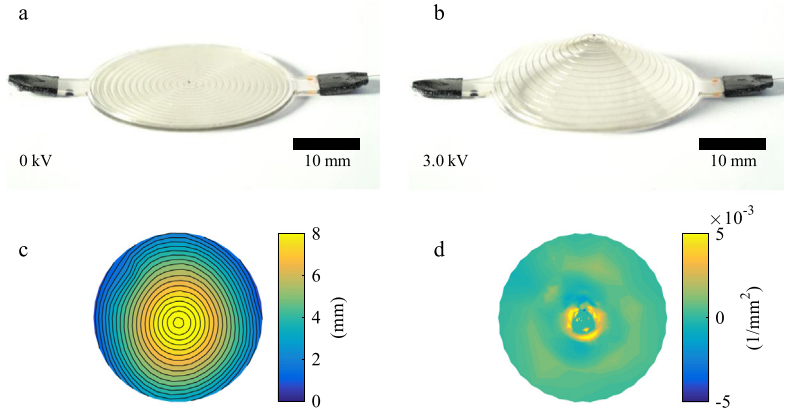

Fig. 2. A dielectric elastomer sheet with 3D-printed stiff concentric rings actuating into a conical surface upon applying a voltage to its inter-digited electrodes. (a and b) optical images of the dielectric elastomer sheet before and after applying 3 kV, respectively. (c) height profile of the actuated dielectric elastomer under 3 kV showing equally-spaced concentric circular contour lines which characterizes a cone shape. (d) Gaussian curvature of the actuation profile, showing large positive curvature at the center and negligible curvature elsewhere, confirming that the actuation shape is a cone.

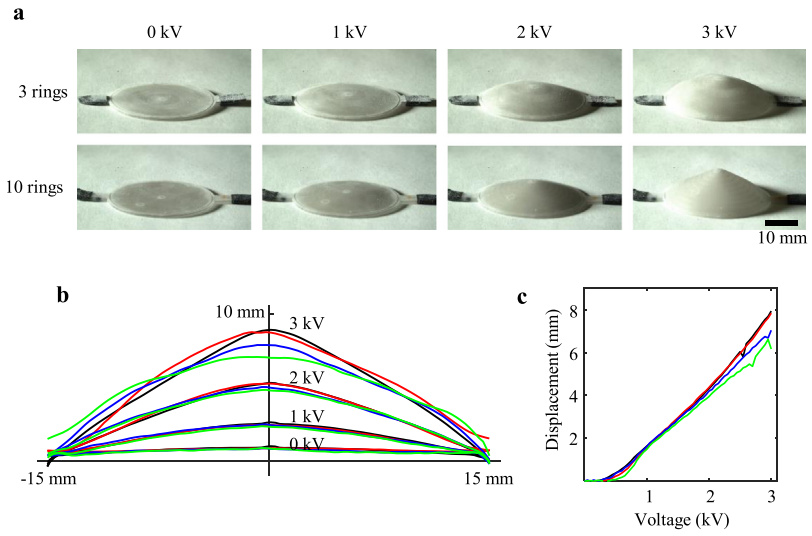

Fig. 3. Actuation of DEAs with concentric stiff rings. (a) Optical images of DEAs with different number of 3D-printed stiff rings morph into a cone shape whose height increases with the applied voltage. (b) Side-view of the profile of the DEAs with 3, 5, 10, and 15 concentric rings shown in green, blue, red and black, respectively, showing that the morphing shape and displacement is not sensitive to the spacing of the rings. (c) Displacement of the center of the disk of DEA as a function of the applied voltage shows that the DEA remains flat for low applied voltages followed by a sudden out-of-plane deformation that increases linearly with the applied voltage.

Here the geometric parameters of the elastomer sheet are the number active layers n, total number of layers m, radius of the elastomer disk R, and the initial thickness of each elastomer layers t_0. The first invariant of the Cauchy–Green deformation tensors, I_1, is related to the principal stretches through $I_1 = \lambda_1^2 + \lambda_2^2 + \lambda_3^2$. The assumption of uniaxial deformation and the incompressibility of the elastomer lead to $\lambda_2 = 1$ and $\lambda_1\lambda_3 = 1$, respectively. Therefore, the first invariant of the Cauchy–Green deformation tensor in terms of the lateral expansion ratio $\lambda = \lambda_1$ is $I_1 = \lambda^2 + 1 + \lambda^{-2}$. The electric field, E, could be expressed in terms of the applied voltage, ϕ, the initial thickness of elastomer layers, and the lateral stretch: $E = \phi\lambda/t_0$. The total charge drawn from the charging unit is $q = n\pi R^2\lambda\epsilon E$. Substituting I_1, E, and q into the total potential energy and minimization of the total potential energy gives an expression for the lateral expansion in terms of the geometrical and material parameters and the applied voltage:

$$\lambda = \left(1 - \hat{E}^2\right)^{-1/4}$$

where $\hat{E} = \sqrt{n/m}\sqrt{\epsilon/\mu}\frac{\phi}{t_0}$ is a normalized electric field. Assuming that under this lateral expansion the elastomer sheet morphs into a cone, the vertical displacement, $z\,(r)$, at distance r from the axis of the cone satisfies $z\,(r)^2 + (R-r)^2 = \lambda^2\,(R-r)^2$. Therefore, the analytical expression for the height profile is

$$z\,(r) = (R-r)\left(\left(1-\hat{E}^2\right)^{-1/2} - 1\right)^{1/2}$$

Fig. 4b compares the analytical profile to the numerical and experimental model, using the same material and geometrical parameters as the ones used for the numerical model. The close agreement between this simple analytical model and the experimental and numerical results confirms the validity of the assumptions. This analytical model could potentially be used for solving the inverse problem of design, in which the design of the rings and electrodes are sought for to achieve a desired pre-defined deformation.

For dielectric elastomer actuators, the actuation force is important in determining their possible applications. A map of the actuation forces as a function of applied voltage and displacement is measured for a dielectric elastomer actuator with ring-spacing of 1 mm and diameter of 30 mm, as described in Characterization.

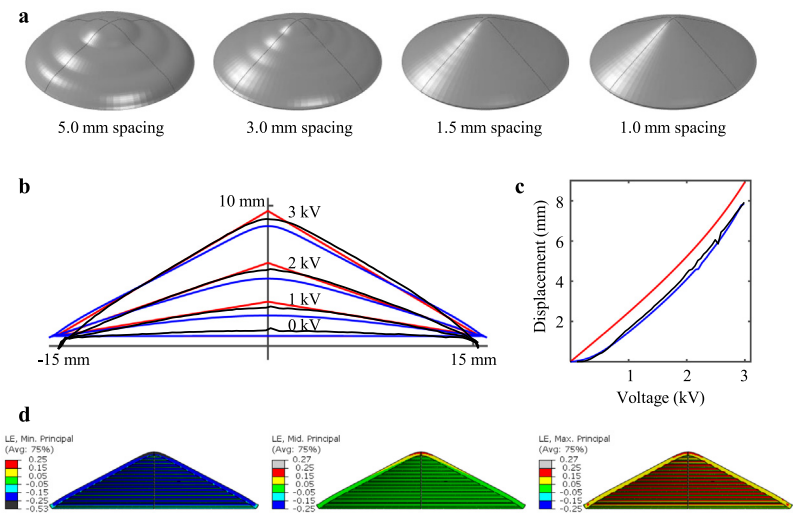

Fig. 4. Comparison of the experimentally measured actuation profiles with those of the numerical and analytical models. (a) Numerical analysis of the actuation shape of the dielectric elastomer sheets with ring-spacings of 1 to 5 mm, under an applied voltage of 3 kV (b) Cross-section profile of the actuator under 1, 2, and 3 kV, calculated using the numerical and analytical models, shown with blue and red lines, respectively, compared to the experimental measurements, shown with black lines. (c) Vertical displacement of the center of the disk of elastomer as a function of the applied voltage, calculated using the numerical and analytical models and compared to the experimental measurements, shown in blue, red, and black, respectively. (d) Numerical results for the distribution of the minimum, intermediate, and maximum principal strains, from left to right, respectively, shown on the cross-section of the actuator under an applied voltage of 3 kV.

As shown in Fig. 5a, an actuation force of half a Newton could be produced with an actuator that is thinner than 1 mm. Unlike the linear dielectric elastomer actuators [20], the maximum actuation force is not the blocking force at zero displacement but it rather maximizes after some actuation displacement, about 1 mm in this case. The numerical analysis of the actuation forces shows a similar trend, Fig. 4b. In this numerical analysis, the friction forces and electro-adhesion between the elastomer surfaces and the plates that are pressing onto it are neglected, which contributes to the difference between the numerical calculations of the actuation forces and the experimental measurements.

The actuation force could also be estimated using the analytical model, following a similar approach used for calculating the actuation displacement. When a force of F is applied to the vertex of the cone shape of the actuator in the opposite direction of the actuation displacement, the work potential of $F\Delta z$ is added to the potential energy, where $\Delta z = R\sqrt{\lambda^2 - 1}$ is the displacement of the vertex of the cone:

$$W = \pi R^2 m t_0 \left(\frac{\mu}{2}(I_1 - 3)\right) + \pi R^2 n t_0 \left(\frac{1}{2}\epsilon E^2\right) - q\phi + F\Delta z$$

Minimization of the total potential energy, $\partial W/\partial\lambda = 0$, results in the following expression for the normalized force as a function of the normalized electric field, $\sqrt{n/m}\sqrt{\epsilon/\mu}\frac{\phi}{t_0}$, and normalized displacement, $\Delta z/R$.

$$\frac{R}{\mu\left(\pi R^2 m t_0\right)}F = \frac{\Delta z}{R}\left(\frac{n}{m}\frac{\epsilon}{\mu}\frac{\phi^2}{t_0^2} + \left(1 + \left(\frac{\Delta z}{R}\right)^2\right)^{-2} - 1\right)$$

Fig. 5c shows the actuation force estimated by the analytical model. The difference between the actuation force estimated by the analytical model and the experimentally measured forces is mainly caused by the assumption made for the derivation of the analytical model, namely that the actuation shape remains a cone even when a force of F is applied. The experiment, however, does not verify this assumption.

Although the exact value of the actuation forces from the analytical model and the experimental measurements are somewhat different, the general shape of the two maps and the order of magnitude of the forces are similar. The analytical model assumes that pressing the stiff plate onto the actuator does not change its cone shape but only the height of the cone, whereas in the experiments the shape of the actuator diverges from a cone when the stiff plate is pressed onto it to make the force measurement, as shown in the Supplementary video 2. This simplifying assumption that the cone remains a cone in the analytical model contributes to the difference between the calculated and measured actuation forces. Nevertheless, the analytical model for the actuation force can be used as a reasonable estimate of the actuation forces as well as to understand the scaling of the actuation force with the geometrical and materials parameters, and with the applied voltage. The analytical model further suggests that for a constant normalized electric field and relative displacement, the actuation force scales linearly with the shear modulus, the volume of the elastomer sheet, and the inverse of the radius of the circular sheet. The experimental observation that the maximum force is not the blocking force at zero displacement is also captured by the analytical model.

Finally, although this work has been concerned with concentric rings as stiffening elements, other stiffening geometries can be employed to create other 3D morphing shapes. A few examples of which are represented in Fig. 6. The first example in Fig. 6 is a set of non-concentric rings for which the elastomer sheet morphs into an oblique circular cone upon applying a voltage of 2.5 kV. The second example is a set of radial stiffening elements constraining the radial stretch and only allowing azimuthal expansion. This state of deformation results in a saddle-like anti-cone shape, as shown in the second column of Fig. 6. This agrees with the nonlinear elasticity of incompatible surface growth [19], predicting that constraining the radial expansion and allowing azimuthal expansion results in an anti-cone shape shown in Fig. 6. The third example is four sets of concentric ring segments, for which the morphing shape is shown on the third column of Fig. 6.

5. Conclusion

A flat multilayered sheet of dielectric elastomer with internal inter-digited electrodes and a set of external 3D-printed stiff concentric rings morphs into a cone shape, fast and reversibly, when a voltage is applied to the inter-digited electrodes. The actuation

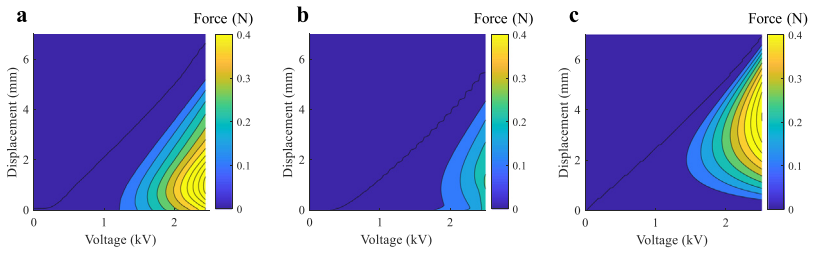

Fig. 5. Two-dimensional map of the actuation force as a function of the applied voltage and displacement for a 31 mm diameter and 0.73 mm thick sheet of dielectric elastomer with 15 concentric rings from (a) the experimental measurements, (b) numerical analysis, and (c) analytical model.

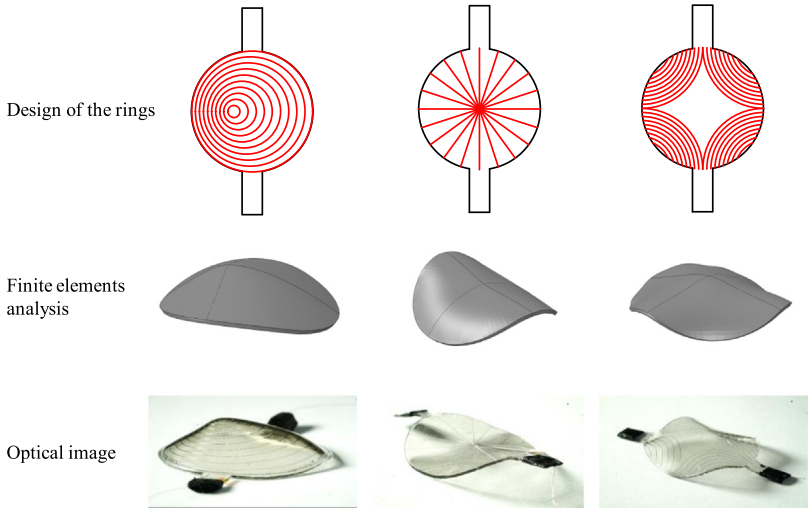

Fig. 6. Examples of designs of 3D-printed stiffening elements and the resulting actuation shapes. The first row shows the design of the stiffening elements, shown by red lines, and the boundary of the actuator, the black lines. The numerical analysis and the optical images of the actuation shapes under 2.5 kV are shown in the second and the thirds rows, respectively.

displacement can be more than ten times the thickness of the disk of elastomer and more than half of its radius. The actuator can provide an actuation force of more than half Newton, which could be optimized for much larger values. The actuation displacement and forces can be accurately predicted using a finite elements user subroutine. The finite elements analysis also shows that the actuation is uniaxial, and the bending terms are negligible. These two findings were used as the assumptions of an analytical model which can also accurately predict the actuation displacements and estimate the actuation forces. The use of 3D-printed rings for guiding the actuation deformation of dielectric elastomers is not limited to the concentric rings with an actuation shape of a cone surface, but a myriad of other designs is possible, as exemplified in this work, and could be pursued further.

Acknowledgments

This work was supported by the MRSEC, USA through the National Science Foundation grant DMR 14-20570. Eesha Khare's work as an undergraduate was supported by the National Science Foundation, USA through the grant CMMI-1333835. We would like to acknowledge Arda Kotikian for useful discussions about acrylate inks.

Declaration of competing interest

The authors declare that they have no known competing financial interests or personal relationships that could have appeared to influence the work reported in this paper.

Appendix A. Supplementary data

Supplementary material related to this article can be found online at https://doi.org/10.1016/j.eml.2019.100504.

References

[1] R. Pelrine, et al., High-speed electrically actuated elastomers with strain greater than 100%, Science 287 (5454) (2000) 836–839.
[2] M. Duduta, et al., Realizing the potential of dielectric elastomer artificial muscles, Proc. Natl. Acad. Sci. (2019) 201815053.
[3] C. Jordi, S. Michel, E. Fink, Fish-like propulsion of an airship with planar membrane dielectric elastomer actuators, Bioinspiration Biomimetics 5 (2) (2010) 026007.
[4] F. Berlinger, et al., A modular dielectric elastomer actuator to drive miniature autonomous underwater vehicles, in: 2018 IEEE International Conference on Robotics and Automation (ICRA), IEEE, 2018.
[5] S. Shian, R.M. Diebold, D.R. Clarke, Tunable lenses using transparent dielectric elastomer actuators, Opt. Express 21 (7) (2013) 8669–8676.
[6] M. Matysek, et al., Dielectric elastomer actuators for tactile displays, in: EuroHaptics Conference, 2009 and Symposium on Haptic Interfaces for Virtual Environment and Teleoperator Systems. World Haptics 2009. Third Joint, IEEE, 2009.
[7] P. Lotz, M. Matysek, H.F. Schlaak, Peristaltic pump made of dielectric elastomer actuators, in: SPIE Smart Structures and Materials+ Nondestructive Evaluation and Health Monitoring, International Society for Optics and Photonics, 2009.
[8] S. Shian, K. Bertoldi, D.R. Clarke, Dielectric elastomer based "grippers" for soft robotics, Adv. Mater. 27 (43) (2015) 6814–6819.
[9] J. Kim, et al., Designing responsive buckled surfaces by halftone gel lithography, Science 335 (6073) (2012) 1201–1205.
[10] T.H. Ware, et al., Voxelated liquid crystal elastomers, Science 347 (6225) (2015) 982–984.
[11] T.J. White, D.J. Broer, Programmable and adaptive mechanics with liquid crystal polymer networks and elastomers, Nature Mater. 14 (11) (2015) 1087.

[12] E. Hajiesmaili, D.R. Clarke, Reconfigurable shape-morphing dielectric elastomers using spatially varying electric fields, Nature Commun. 10 (1) (2019) 183.
[13] M. Duduta, R.J. Wood, D.R. Clarke, Multilayer dielectric elastomers for fast, programmable actuation without prestretch, Adv. Mater. 28 (36) (2016) 8058–8063.
[14] S. Shian, et al., Highly compliant transparent electrodes, Appl. Phys. Lett. 101 (6) (2012) 061101.
[15] M.J. O'connell, et al., Band gap fluorescence from individual single-walled carbon nanotubes, Science 297 (5581) (2002) 593–596.
[16] T. Lu, et al., Dielectric elastomer actuators under equal-biaxial forces, uniaxial forces, and uniaxial constraint of stiff fibers, Soft Matter 8 (22) (2012) 6167–6173.
[17] N.H. Ismail, M. Mustapha, A review of thermoplastic elastomeric nanocomposites for high voltage insulation applications, Polym. Eng. Sci. 58 (S1) (2018) E36–E63.
[18] D.L. Henann, S.A. Chester, K. Bertoldi, Modeling of dielectric elastomers: Design of actuators and energy harvesting devices, J. Mech. Phys. Solids 61 (10) (2013) 2047–2066.
[19] L. Truskinovsky, G. Zurlo, Nonlinear elasticity of incompatible surface growth. arXiv preprint arXiv:190106182, 2019.
[20] H. Zhao, et al., Compact dielectric elastomer linear actuators, Adv. Funct. Mater. 28 (42) (2018) 1804328.